Please cite the Published Version

Original Article

Crystalline TiO₂ supported on stainless steel mesh deposited in a one step process via pulsed DC magnetron sputtering for wastewater treatment applications

Matthieu Grao[a], Marina Ratova[a,*], Camila C. Amorim[b],
Rafaela B.P. Marcelino[b], Peter Kelly[a]

[a] Manchester Metropolitan University, All Saints Building, All Saints, Manchester M15 6BH, United Kingdom
[b] Federal University of Minas Gerais, Av. Pres. Antônio Carlos, 6627 - Pampulha, Belo Horizonte - MG, 31270-901, Brazil

ARTICLE INFO

ABSTRACT

TiO₂ thin films were deposited on woven stainless-steel mesh by pulsed DC magnetron sputtering, at room temperature without substrate bias or annealing. Woven stainless-steel mesh is inexpensive, flexible, semi-transparent and has a high surface area. This coating/substrate combination was selected for future photocatalytic reactor integration. The effect of operating pressure and magnetron power on coating crystallinity and photocatalytic activity were investigated. Results indicate that magnetron power is a key factor, as it affects the crystallinity and morphology of the thin films. A combination of low pressure and high-power lead to a one-step synthesis of TiO₂ coatings with a mixed anatase and rutile phase. An optimised sample was produced and tested for methylene blue, methyl orange and rhodamine B decomposition under UV-A. Using various trapping agents, •OH and O_2^{-}• radicals were identified as the main photogenerated species responsible for the model pollutant degradation. Finally, durability tests revealed little to no photocatalytic performance deterioration after ten repeated cycles. This confirmed the suitability of this coating/substrate combination for future photocatalytic reactor integration.

https://doi.org/10.1016/j.cviu.2017.00.000

1. Introduction

It was estimated that, in 2015, 844 million people still lacked basic access to drinking water, while 711 million people used inadequately treated sewer connections [1]. As a result, one child dies from contaminated water every two minutes [2]. These deaths are preventable and highlight the need for new and reliable methods to treat unsanitary water. Photocatalysis is an advanced oxidation process, which uses solar energy to mineralise organic compounds. It is a cost effective, simple and sustainable method for water or air purification [3].

To date, the most widely used photocatalyst remains crystalline titanium dioxide, whose properties were discovered by Fujishima and Honda in 1969 [4]. When irradiated by a light source with an energy equal or greater to its bandgap (3.20 eV) [5], crystalline titanium dioxide generates electron-hole pairs. These excitons react at the surface of TiO_2, with surrounding molecules to form reactive species, such as hydroxyl ($\bullet$OH) and superoxide ($\bullet O_2^-$) radicals, capable of mineralising organic compounds. TiO_2, also known as titania, is non-toxic, stable, inexpensive and has been widely used for various applications, such as water electrolysis, dye-sensitised solar cells, air/water purification, self-cleaning coatings, non-spotting glass, self-sterilising coatings, etc. [6–11].

TiO_2 thin films can be produced via chemical vapor deposition, sol-gel, pulsed laser deposition, solvothermal synthesis, etc. [12–15]. TiO_2 and other photocatalysts are often produced and tested as powders [16–18]. Although efficient, the treated wastewater must be separated from the photocatalytic powder, with expensive membranes, to recover the photocatalyst and safely discharge the treated water.

Reactive magnetron sputtering (RMS) has the advantage of directly immobilising the catalyst on the substrate, facilitating the catalyst recovery. This process is reproducible, scalable, produces uniform films and provides great control over chemical and morphological properties [19]. Unfortunately, TiO_2 thin films deposited by RMS are often amorphous when produced without substrate bias [20], radio frequency power supplies [20,21], substrate heating [22] or post-annealing [23–25].

Ratova et al., successfully deposited anatase on glass via RMS without any of these, using relatively elevated working pressures to drive the sputtering process [26]. Herein, a similar set of conditions were used to not only investigate the influence of pressure, but also power, on the crystallisation process.

Stainless steel 304 L woven mesh was chosen as a substrate, for its high surface area, low cost, flexibility, porosity to light and tolerance for high temperatures [3]. This coated stainless steel mesh could easily be integrated in a compound parabolic collector, for efficient photocatalytic waste water treatment [27,28]. As the substrate is semi-transparent, several layers of mesh could be stacked inside the photoreactor, to increase the catalyst load whilst maintaining light permeability.

Herein, the crystallinity and photocatalytic activity of 9 samples, coated at varying levels of working pressure and power were investigated. Consequently, an optimised sample was prepared under working pressure and power conditions believed to maximise photocatalytic activity. This optimised sample was tested for methylene blue (MB), methyl orange (MO) and rhodamine B (RhB) degradation under UV-A. These dyes respectively belong to the xanthene, azo and thiazine families and account for almost 90% of the research, in the field of dye photodecomposition. Evaluating the performance of a photocatalyst using a single dye does not validate the performance of a photocatalyst in real-world conditions [29]. Testing a set of different dyes partially negate this effect and is, therefore, recommended to confirm the efficiency of a photocatalyst.

The present work describes a parametric study of TiO_2 deposition on woven stainless-steel mesh via pulsed DC RMS. Herein, a combination of high sputtering power and low operating pressure were identified as the optimum conditions, to obtain a mixture of anatase and rutile titanium dioxide, in a one-step process. Obtaining such coatings on woven stainless-steel mesh, without post treatment or expensive equipment could provide a route towards high scale production of stainless-steel mesh-based photocatalytic reactors.

2.   Materials and methods

2.1.   Deposition

Titanium dioxide thin films were deposited with a Nordiko sputtering rig [30] (schematic representation of the rig is given in Figure S1, Supplementary material), under a high vacuum, achieved through a combination of rotary (BOC Edwards 80) and turbo molecular (Leybold TMP1000) pumps. A single 300×100 mm titanium target (99.5% purity) was fitted on a Gencoa Ltd unbalanced type II magnetron [19]. The distance between the target and the substrate was 50 mm. The argon flow rate was kept constant at 50 sccm for all deposition runs. The oxygen flow was regulated by a Speedflo®™ controller from Gencoa Ltd, to produce stoichiometric films whilst minimising target poisoning. The magnetron was powered by an Advanced Energy Pinnacle Plus power supply, in pulsed DC mode, operating at a frequency of 100 kHz and 60% duty. TiO_2 thin films were deposited onto square sheets of stainless-steel 304 L mesh (3×3 cm^2), with an aperture of 0.41 mm and a wire diameter of 0.22 mm; the substrate was ultrasonically pre-cleaned in acetone. All chemicals used were purchased from Sigma Aldrich, unless stated otherwise. Power delivered to the target and the operating pressure, were varied along three levels, as described in Table 1. The samples were produced in the following randomized order: No. 3, 4, 5, 1, 9, 8, 6, 2 and 7 and the deposition time was fixed at two hours. The chamber pressure was varied by adjusting the aperture of the

Table 1 – Parameters used for each deposition.

Sample	Pressure (Pa)	Power (W)
No.1	0.44	250
No. 2	0.44	500
No. 3	0.44	750
No. 4	1.77	250
No. 5	1.77	500
No. 6	1.77	750
No. 7	3.10	250
No. 8	3.10	500
No. 9	3.10	750
No. 10	0.44	1000

gate valve between the turbomolecular pump and the chamber. These power and pressure ranges were chosen to ensure plasma stability. An additional optimised coating, termed No. 10, was produced under conditions predicted to yield superior photocatalytic activity.

2.2. Characterisation

The thin film morphology was evaluated by scanning electron microscopy (SEM) using a Zeiss Supra 40 VP-FEG-SEM. The composition was determined by energy-dispersive X-ray spectroscopy (EDX), with an EDAX Trident system installed on the FEG-SEM. Strands of the mesh were partly cut through and subsequently fractured to reveal their cross-sections and measure the coatings' thicknesses. The thin films' crystallinity was assessed by X-ray diffraction (XRD), on a Panalytical Xpert system. CuK_{α} radiation at 0.154 nm was used, in grazing incidence mode at $3°$, over a scan range from 20 to $70°$ 2θ. The accelerating voltage and applied current were set to 40 kV and 30 mA respectively. Raman mapping was performed on samples determined to be crystalline by XRD, with a DXR Raman microscope from Thermo Scientific. The laser was operated at a wavelength of 532 nm, with a power of 10 mW, 900 lines per mm grating, a long working distance microscope objective with magnification of 50, an estimated spot size of 1.1 μm and a 25 μm pinhole. 1677 Raman spectra were acquired using a step size of 100 μm along the Y and X axes. The oxidation state information was obtained using X-ray photoelectron spectroscopy (XPS), performed with an AMICUS photoelectron spectrometer (Kratos Analytical Ltd.) equipped with Mg K X-rays as the primary excitation source. The binding energy was referenced to the C 1s line at 284.8 eV for calibration. Curve fitting was performed applying a Gaussian function with a Shirley background. The average roughness (Ra) of the coated and uncoated stainless-steel mesh samples were measured using a white light interferometer Profilm3D from Filmetrics, with a magnification of 50. Three images were obtained on random areas of the mesh and were averaged to find the Ra (ISO 4287).

2.3. Methylene blue degradation

The photocatalytic properties of the produced samples were first assessed and compared by monitoring their ability to degrade methylene blue (MB), under UV-A light. Schematic representation of the testing set-up and emission spectrum of the light source used are given in the Figures S2 and S3 of Supplementary material, respectively. In brief, samples were placed on top of a sample holder, in a quartz cuvette filled with 50 mL of methylene blue solution (2 μmol/L), purchased from Alfa Aesar. The samples were left in the dark for 60 min under continuous stirring, to reach adsorption-desorption equilibrium. Then, they were irradiated by a UV-A source (2 × 15 W Sankyo Denki BLB lamps, peaked at 365 nm) for 60 min. The source's integrated irradiance was measured at 273 W/m^2. The methylene blue main absorption peak (664 nm) was monitored with an Ocean Optics USB4000 UV–vis spectrometer. The pseudo-first-order rate constant k_{α} was obtained by plotting $Ln(A_0/A_t)$ against the time, by calculating the gradient of the plot [26]. The obtained k_{α} values were used to compare the photocatalytic activity of each sample.

2.4. Investigation of the photogenerated species via trapping reactions

The optimised sample No.10 was tested for its ability to degrade methyl orange (MO), in the presence of different scavengers. The following trapping agents were employed: isopropanol for •OH [31–33], 4-hydroxy TEMPO for $O_2^{-•}$ [31,34], sodium oxalate for h$^+$ [35,36] and sodium nitrate for e- [37]. Methylene blue having a complementary colour to 4-hydroxy TEMPO, it formed a green solution when mixed. To prevent possible self-photosensitization effects due to coloured substance interactions [38], methyl orange (MO) was chosen instead. Sample No. 10 was placed on top of a sample holder in a quartz cuvette, immersed in a 50 mL solution of methyl orange (1.5 μmol/L) in the presence of each scavenger (7 mmol/L). The sample was left in the dark for 60 min under continuous stirring, to reach adsorption-desorption equilibrium. The same irradiation source described in 2.3, was used to illuminate the sample for 1 h. The main absorption peak of methyl orange (465 nm) was monitored with an Ocean Optics USB4000 UV–vis spectrometer.

2.5. Reusability assessment

The reusability of sample No. 10 was evaluated by testing its ability to degrade rhodamine B (RhB), a dye known to be more resilient to photocatalytic degradation than methylene blue [39]. Afterwards, the sample was washed with distilled water, dried with compressed air and the operation was repeated with the same sample 9 more times. Sample No. 10 was placed on top of a sample holder, in a 100 mL beaker and immersed in a 50 mL solution of rhodamine B (2 μmol/L). The sample was left in the dark for 60 min under continuous stirring, to reach adsorption-desorption equilibrium. The same irradiation source, as described in 2.3, was used to irradiate the sample for 1 h. The main absorption peak of rhodamine B at 554 nm was measured before and after UV-A exposition with a Cary 300 UV–vis spectrophotometer.
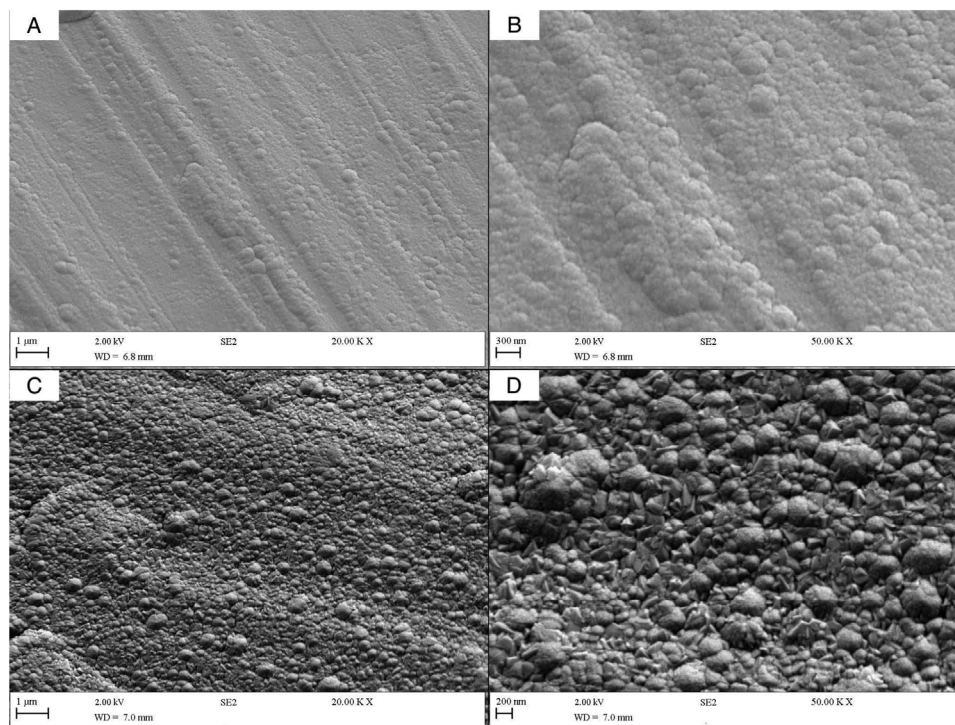
Fig. 1 – FE-SEM micrographs at different magnifications of (A, B) sample No. 3 (500 W – 1.77 Pa) and (C, D) sample No. 5 (750 W – 0.44 Pa), TiO$_2$ thin films on woven stainless-steel mesh prepared by RMS.
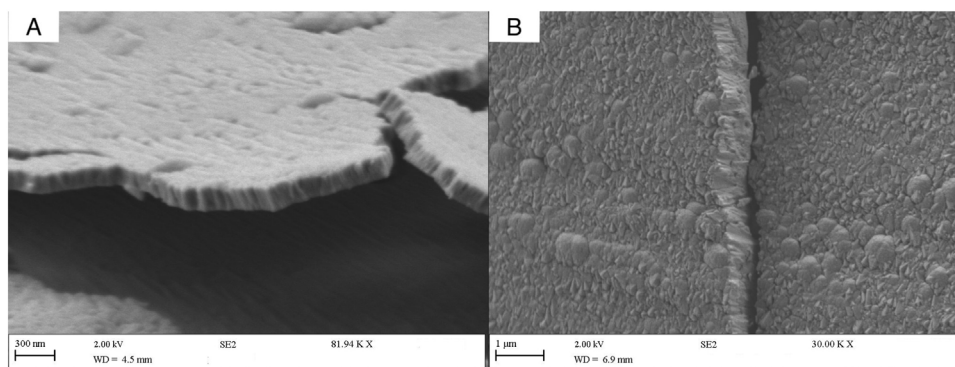

Fig. 2 – FE-SEM micrographs of the cross-section of (A) sample No. 3 (500 W – 1.77 Pa) and (C, D) sample No. 5 (750 W – 0.44 Pa), TiO$_2$ thin films on woven stainless-steel mesh prepared by RMS.

3.   Results and discussion

3.1.   Characterisation of TiO$_2$ coated mesh samples

Scanning electron microscopy revealed the presence of two distinct coating morphologies. The first one, observed for samples No.1, 2, 4, 5, 6, 7, 8 and 9 is a dense cauliflower-like structure, as illustrated by the surface micrograph of sample No. 5 prepared at 500 W – 1.77 Pa (Fig. 1A, B). The second morphology, only observed in sample No. 3 (750 W – 0.44 Pa), is a dense mixture of cauliflower-like and crystal-like features (Fig. 1C, D). A dense columnar structure was identified across all samples, as shown for samples No. 3 and No. 5 (Fig. 2).

The substrate was identified as a mixture of Fe$_{4.00}$ and Fe$_{2.00}$ from the JCPDS cards 96-900-8470 & 96-901-3476, respectively (Fig. 3). Crystalline TiO$_2$ diffraction peaks were only identified in sample No.3 (Fig. 3). Anatase peaks at 25.4° (101), 37.9° (004), 53.9° (105) and 55.3° (211) were identified with the JCPDS card 96-720-6076, while a rutile peak was identified at 27.4° (110) with the JCPDS card 96-900-4145. The other samples did not show any detectable peaks, which may indicate that they are amorphous or nanocrystalline, with crystallites below the detection limit of the XRD system used here.

The Raman mapping performed on sample No. 3 (750 W – 0.44 Pa) revealed the presence of anatase on every thread of the stainless-steel mesh (Fig. 4). The coating seems to be homogeneously distributed, despite the substrate's complex
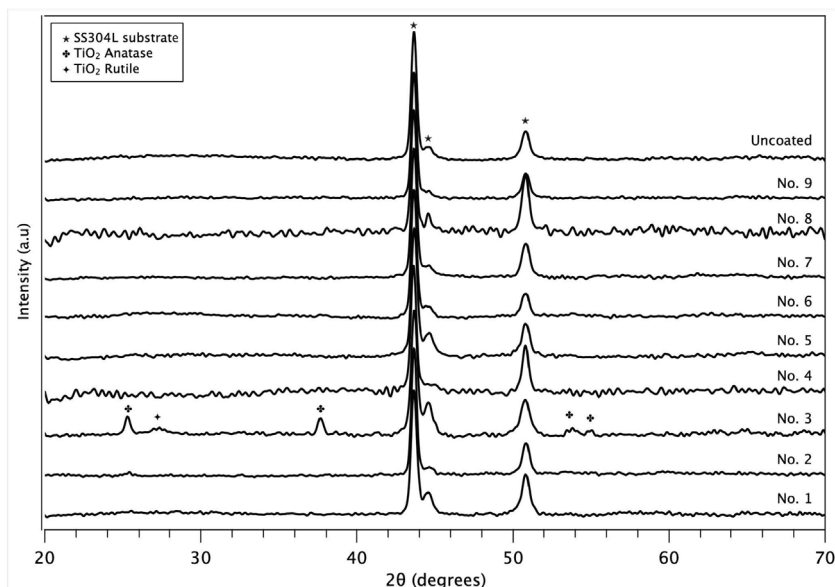
Fig. 3 – XRD patterns of TiO₂ thin films deposited onto stainless steel mesh.
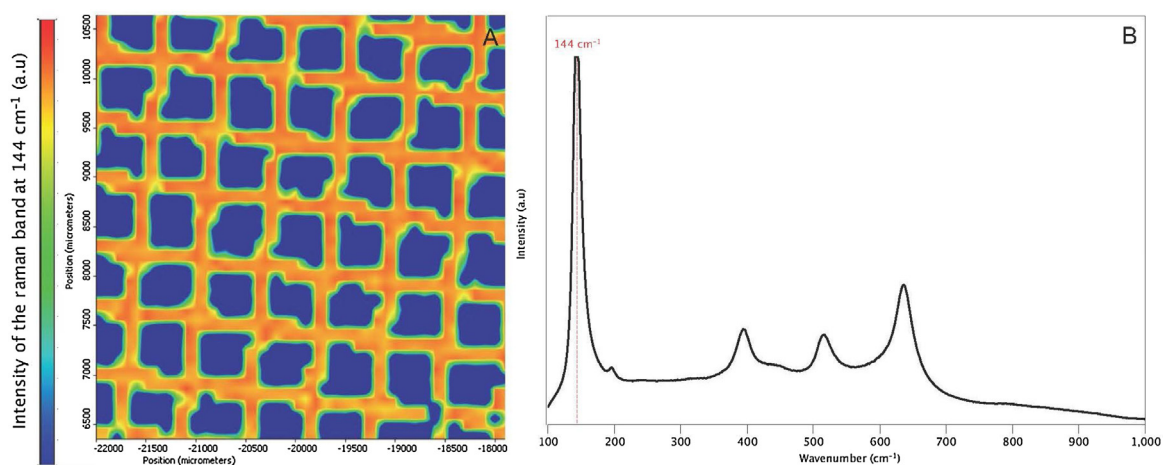

Fig. 4 – Raman mapping sample No.3 produced at 750 W – 0.44 Pa (A) corresponding Raman spectrum (B).

geometry. This analysis was not performed on other samples because of their amorphous or nanocrystalline nature.

Chemical states of the elements were studied with X-ray photoelectron spectroscopy; Gaussian functions were used for deconvolution of the individual peaks. Selected examples of the elements XPS spectra for sample No. 3 (750 W – 0.44 Pa) and No. 7 (250 W – 3.10 Pa) are presented in Fig. 5A, D. As expected, survey spectra of both samples No. 3 (Fig. 5A) and No. 7 (Fig. 5D), only revealed Ti 2p, O 1s and C 1s peaks. The latter one is due to adventitious carbon on the surface; the binding energies of the other elements were referenced to this peak at 284.8 eV. High resolution spectra of the Ti 2p shown in Fig. 5B and E of samples No. 3 and No. 7, respectively, had no significant variations, regardless of the sputtering conditions used. On these spectra of Ti 2p, the peak positioned at 458.3 eV corresponds to Ti $2p_{3/2}$, while the peak at 464.1 eV can be assigned to Ti $2p_{1/2}$; the positions of both peaks are in good

agreement with the positions of Ti in TiO_2, indicative of the fact that Ti atoms are in the form of the Ti^{4+} valence state. High resolution spectra of O 1s of selected samples No. 3 and No. 7 are given in Fig. 5C and F, respectively. All high-resolution oxygen spectra can be deconvoluted into two peaks, where the peak at 529.5 ± 0.3 eV can be attributed to the lattice oxygen and the peak at 531−533 eV (marked O_a in Fig. 5) is typically attributed to the presence of adsorbed O_2 and/or H_2O (−OH) on the surface of TiO_2 films [40,41]. It is evident that increasing the power applied to the titanium target to 750 W for sample No. 3 resulted in increased intensity of the lower binding energy peak and weaker adsorbed oxygen peak. This can be used as a confirmation of the fact that higher sputtering powers lead to more energetic conditions at the substrate and therefore transformation of adsorbed oxygen into Ti-O bonds; similar phenomenon was reported by Zhou et al. [41] who studied preparation of TiO_2 by thermal oxidation of sputtered tita-
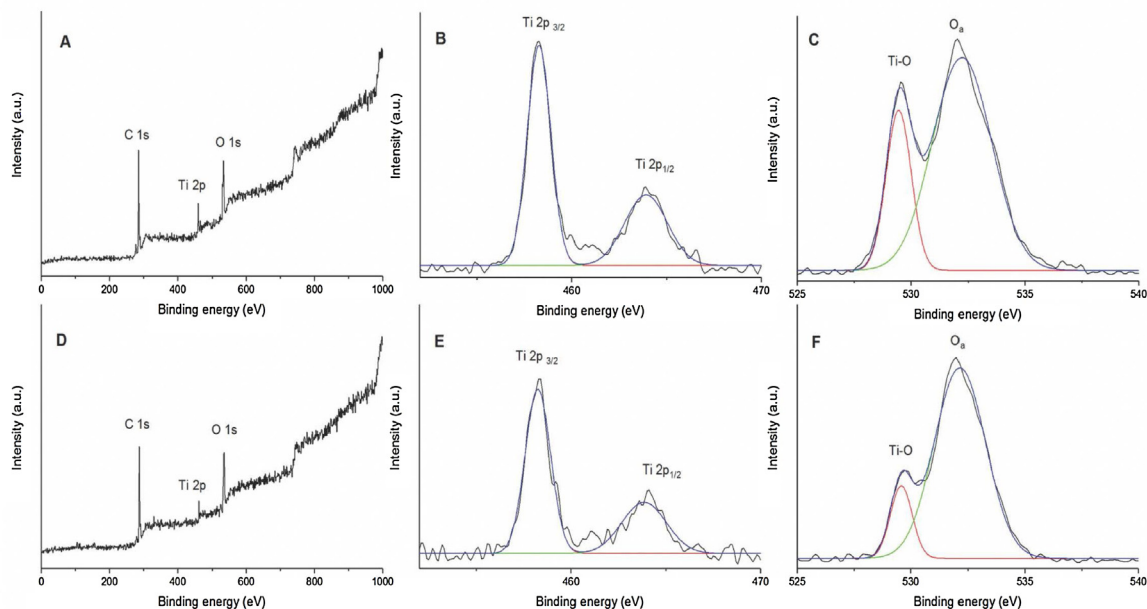
Fig. 5 – Selected XPS spectra of titanium dioxide coatings: (A) survey spectrum of sample No. 3; (B) Ti 2p spectrum of sample No. 3; (C) O 1s spectrum of sample No. 3; (D) survey spectrum of sample No. 7; (E) Ti 2p spectrum of sample No. 7; (F) O 1s spectrum of sample N. 7.
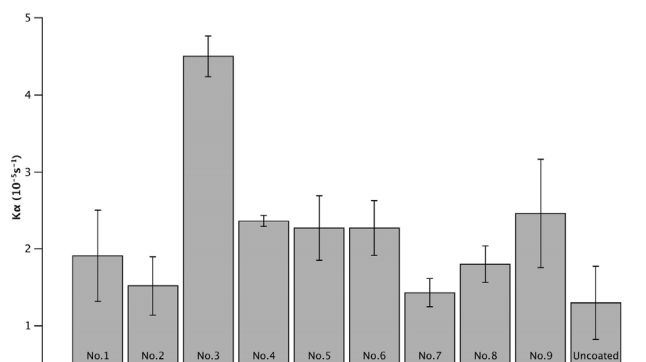

Fig. 6 – MB pseudo first rate order degradation kinetics calculated for every TiO$_2$ coated and uncoated woven stainless-steel mesh samples.

nium. A similar trend in high resolution spectra of oxygen (decrease of absorbed oxygen peak with increased sputtering power) was observed for the other studied samples (results are not shown).

3.2. Photocatalytic activity evaluation of the TiO$_2$ coated mesh samples

Table 2 summarises the studied properties of the uncoated and TiO$_2$ coated stainless steel mesh samples. When considering 9 combinations of the variable sputtering conditions, sample No. 3 stands out as the only crystalline sample, which explains its significantly higher MB degradation rate (Fig. 6). As shown in Table 2, the measured thickness of the coated mesh varied from < 200 nm to > 800 nm. The measured roughness of the samples was of the same magnitude as the uncoated

mesh. Therefore, the photocatalytic performances of the coatings were compared directly with no additional factor required for the effect of surface area. The results seem to suggest that increasing the target power and reducing the operating pressure tend to favour the crystallisation of TiO$_2$, with an associated increase in photocatalytic activity. Although no XRD peaks were observed for all runs except sample No. 3, the fact that photocatalytic activity was measured for the other samples does suggest that they may possess nano crystallites (Figs. 7 and 8).

3.3. Crystallisation process investigation

During RMS deposition, the growing film is bombarded with energetic ions from the plasma. Substrate bombardment by high energy ions can provide sufficient mobility to the sputtered adatoms, to produce crystalline thin films without additional substrate heating [42,43]. Alfonso et al. studied the crystallinity of ZrN_xO_y thin films sputtered at different powers and, similarly to our results, found out that a power threshold had to be reached to obtain a crystallised structure. This effect was attributed to the increased ion bombardment [43].

To investigate this, the current drawn at the substrate holder during selected run conditions was estimated using a biased probe. For each set of conditions, the bias voltage applied to the probe was increased progressively using an Advanced Energy MDX power supply. The current drawn at the substrate was recorded from the power supply. Two sets of conditions were tested; pressure fixed at 0.44 Pa and power varied from 250 to 750 W (Fig. 7A) and power fixed at 750 W and pressure varied from 0.44 to 3.10 Pa (Fig. 7B). According to probe theory [44], without any potential applied to an electrically isolated probe facing a plasma, the net measured current

Table 2 – Overview of the TiO₂ coating properties and photocatalytic activity.

Sample	Thickness (nm)	Ra (μm)	Crystalline phase	k_α (10^{-5} s^{-1})	R^2
Control	–	0.340	–	1.30	0.93
No. 1	0.230	0.460	Amorphous	1.91	0.97
No. 2	0.260	0.290	Amorphous	1.52	0.85
No. 3	**0.830**	**0.140**	**Anatase & rutile**	**4.50**	**0.94**
No. 4	0.180	0.400	Amorphous	2.36	0.96
No. 5	0.150	0.410	Amorphous	2.27	0.96
No. 6	0.540	0.280	Amorphous	2.27	0.99
No. 7	0.310	0.180	Amorphous	1.43	0.96
No. 8	0.510	0.220	Amorphous	1.80	0.86
No. 9	0.600	0.240	Amorphous	2.46	0.95

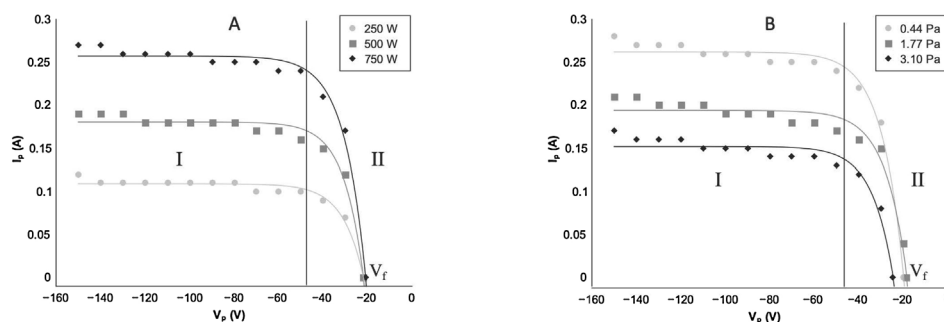The bold value signifies the best performing sample.

Fig. 7 – Plasma I-V characteristics with increasing power (250–750 W) at constant pressure (0.44 Pa) (A) and increasing pressure (0.44–3.10 Pa) at constant power (750 W) (B). (Ip: probe current, Vp: probe voltage, Vf: floating potential, I: ion saturation.
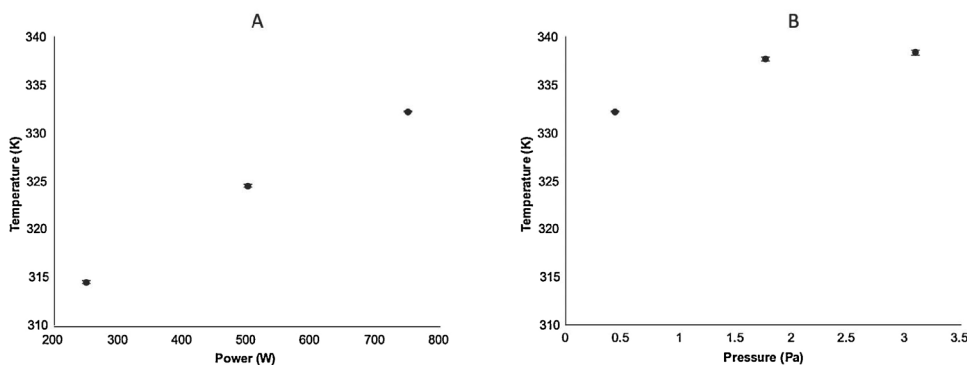

Fig. 8 – Substrate measured temperature with increased power (250–750 W) at constant pressure (0.44 Pa) (A) and increased pressure (0.44–3.10 Pa) at constant power (750 W) (B).

should be null and a floating potential ranging from −20 to −30 V should be measured. The null current is due to an equal number of ions and electrons reaching the probe. The negative potential, also called floating potential V_f, is a result of the self-biasing of the probe, which arises due to the greater e$^-$ mobility, compared to ions. By applying an increasing negative potential to the probe, the electrons are increasingly repelled, which is observed by a greater current drawn by the probe and marks a transition region (II). If the applied potential is sufficiently large, all the electrons are repelled from the probe and only ions are collected in the ion saturation region (I). The current drawn in this region gives an estimate of the ion current incident, at the substrate. The I–V characteristics of the probe revealed an increased ion current with higher target power (Fig. 7A), while an inverse effect was found for higher pressure (Fig. 7B). At high power, the greater ion flux density bombarding the substrate is likely providing enough mobility to the adatoms to form a crystalline structure. On the other hand, at high pressure, the greater amount of gas phase collisions is probably responsible for the loss in ion energy, which may hinder the crystallisation process.

It is widely known that amorphous thin TiO₂ films can be converted into anatase when annealed at temperatures above
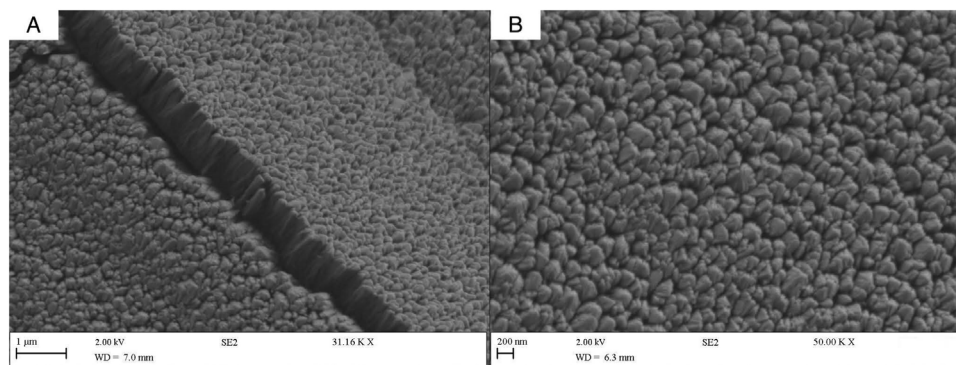
Fig. 9 – Cross-section (A) and top view (B) FE-SEM micrograph of thin TiO$_2$ film No. 10 synthesized at 1000 W – 0.44 Pa onto a stainless-steel mesh substrate by RMS.

673 K [45–,46,47,48,49]. Therefore, the substrate's temperature was measured at equilibrium, using a PicoSens probe from Opsens, with the same two sets of conditions to make sure that there was no direct annealing during the deposition; pressure fixed at 0.44 Pa and power varied from 250 to 750 W (Fig. 8A) and power fixed to 750 W and pressure varied from 0.44 to 3.10 Pa (Fig. 8B). In both cases increasing the power (Fig. 8A) and the pressure (Fig. 8B) did increase the temperature, but not to the same extent, as power seemed to have a greater impact. However, in our set of conditions, the temperature stayed well below the 673 K mark (Fig. 8), which suggests that the crystallisation occurred mainly because of the ion bombardment and not by direct substrate annealing.

Contrary to other studies, increasing the pressure did not increase the photocatalytic activity but had the opposite effect [26,50]. This could be due to the substrate difference; stainless steel was used in present work, while most of earlier reported studies were performed on glass. As for the power, a similar study by Wang et al. found that it was possible to obtain crystalline TiO$_2$, in a one step process on an aluminium alloy substrate, by increasing the magnetron power and substrate bias voltage [51]. This is in accordance with our results, although crystallised TiO$_2$ was obtained in a without substrate bias.

3.4. Optimised sample

To confirm the influence of power and pressure over the coating's properties, a confirmation sample, No. 10, was synthesized. The pressure was set to the lowest achievable value of 0.44 Pa, for which a stable plasma can be obtained (with process gases flows as described in Section 2.1 and gate valve in fully open position). The power was set to 1000 W to confirm the observed effect of higher sputtering power on the films' crystallinity and photocatalytic activity. The resulting sample No. 10, proved to be crystalline as well, outperforming all previous samples and confirming our assumptions on the effects of working pressure and applied power. Further power increases (up to 1.5 kW) were investigated but resulted in films with photocatalytic activity similar to sample No.10, and thus were not included in the presented dataset. Moreover, further increase of the applied power can possibly cause issues with less efficient target cooling and were not consid-
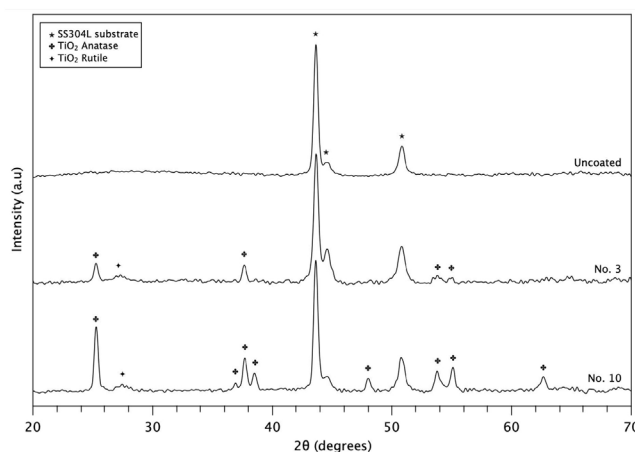

Fig. 10 – XRD patterns of TiO2 thin films on stainless steel mesh synthesized at 750 W – 0.44 Pa (No.3) and 1000 W – 0.44 Pa (No. 10).

ered practical for this system. Sample No. 10 was thoroughly characterised and compared to sample No.3. The optimised sample having the highest photocatalytic activity, it was used to investigate the mechanisms involved in the degradation of a model pollutant (methyl orange). Additionally, the reusability of this optimised sample was evaluated for its ability to degrade rhodamine B, over 10 consecutive cycles.

3.5. Characterisation of the optimised sample

The scanning electron microscopy analysis of the optimised sample No. 10 revealed the disappearance of the cauliflower-like features in favour of angular crystal-like features (Fig. 9A). The coating's columnar profile became more prominent, as revealed by the cross-section shown in Fig. 9B.

The XRD patterns of sample No. 10 are presented in Fig. 10. Just like sample No. 3, the optimised sample has the same anatase peaks at 25.4° (101), 37.9° (004), 53.9° (105) and 55.3° (211) (JCPDS card 96-720-6076) and rutile peak identified at 27.4° (110) (JCPDS card 96-900-4145). The anatase peaks of sample No. 10 became sharper, when compared to sample No. 3. Additionally, new anatase peaks were identified at 37° (103),

Table 3 – Overview of the photocatalytic activity of the optimised sample No. 10 (1000 W - 0.44 Pa) for three different types of dye.

Pollutant	Dye family	Removal % after 1h	k_α (10^{-5} s^{-1})
Methylene blue	Xanthene	18.0 ± 1.7	5.3 ± 0.6
Methyl orange	Azo	17.2 ± 0.7	5.3 ± 0.4
Rhodamine B	Thiazine	11.2 ± 2.9	3.3 ± 0.9

38.6° (112), 48.1° (200) and 62.7° (204) (JCPDS card 96-720-6076), highlighting an increased crystallinity for the optimised sample, produced at a higher power.

The coating's uniformity was assessed by performing a Raman mapping and EDX analysis (summary of the EDX analysis is given in Table S1 of Supplementary material). Analogous to sample No. 3, the Raman mapping performed on sample No. 10 revealed the presence of anatase on every strand of the stainless-steel mesh (Fig. 11). Some small regions may seem uncoated, but in reality, the overlapping of some threads interfered with the microscope focus. To further investigate the quality of the coating, the elemental composition of the coatings was obtained by EDX (Fig. 12) and performed on five different points. A standard deviation <5% was calculated, further confirming the uniformity of the coatings deposited by pulsed DC magnetron sputtering.

The XPS analysis of the optimised sample revealed, as expected, Ti 2p, O 1s and C 1s peaks (Fig. 13). The high-resolution spectra of the Ti 2p of the optimised sample (Fig. 13) did not reveal any significant difference compared to sample No. 3 (Fig. 5). On the other hand, the high-resolution spectra of the O 1s of samples No. 3 (Fig. 5) and No. 10 (Fig. 13) revealed a continuity of the phenomena discussed in 3.1. An increase of power applied to the titanium target resulted in a more intense lower binding energy peak than the adsorbed oxygen peak. This further confirms that a higher sputtering powers results in higher substrate temperatures and therefore transformation of adsorbed oxygen into Ti-O bonds as reported by Zhou et al. [41].

3.6. Photocatalytic activity evaluation of the optimised sample

The optimised sample was tested for the degradation under UV-A of the three most common dyes used in the field of photocatalysis. The summary of the photocatalytic tests is presented in Table 3 and reveals that sample No.10 was able to achieve good levels of degradation for each dye. Compared sample No. 3, the optimised sample degraded MB 18% more effectively. Considering the small surface area of an immobilised photocatalyst, the ability of the optimised sample to degrade rapidly all these model pollutants makes it a good candidate for future photocatalytic reactor integration.

3.7. Investigation of the photocatalytic degradation mechanisms

To understand the mechanism behind the photocatalytic degradation of pollutants, the optimised sample was used to decompose methyl orange (MO) under UV-A in the presence of different trapping agents. 4 hydroxy-TEMPO was used to scavenge superoxide radicals, isopropanol as a hydroxyl radicals' scavenger, sodium oxalate for holes and finally sodium nitrate for electrons. The results of the experiments are given in Fig. 14. When isopropanol and 4 hydroxy-TEMPO were used (Fig. 14C and D, respectively), no dye degradation was observed, suggesting that •OH and $O_2^{-\bullet}$ are the main active species generated on the photocatalysts' surface. In the presence of sodium oxalate (hole scavenger) and sodium nitrate (electron scavenger) no degradation rate change was observed (Fig. 14A and B). The excitons do not seem to directly participate in the degradation of the dye. Therefore, the oxidation pathway may be designated as indirect oxidation [52]. The •OH radicals produced by oxidation of surface hydroxyl or adsorbed water, are known to play an important role in initiating oxidation reactions. It is especially true when the adsorption is negligible, as it is the case in thin films [52].

3.8. Reusability assessment

The durability of sample No.10 was assessed by testing its ability to degrade rhodamine B, under UV-A, during 10 consecutive cycles (Fig. 15). The sample's ability to degrade rhodamine B did not decrease significantly after multiple uses. These results confirm this substrate/catalyst combination's potential, for future integration into a photocatalytic reactor.

4. Discussion

This work demonstrates that crystalline, photocatalytically active, TiO$_2$ thin films can be deposited in a one-step process, on woven stainless-steel mesh substrates. A combination of a low working pressure and high applied power tend to produce the best results in terms of both crystallinity and photocatalytic activity. Ion current measurements suggest that a high ion current is required for crystallisation to occur. Raising the power resulted in an increased ion current drawn at the substrate, while pressure had an opposite outcome. High ion current is believed to improve adatom mobility, facilitating the crystallisation process [43]. However, these results contradict the findings of several authors, who reported previously that using high pressure improved the crystallinity of thin TiO$_2$ films [26,50,53–55]. It should be noted though, the earlier findings were all reported for glass being used as the substrate, while in the current study the coatings were deposited onto stainless steel. This may indicate that the substrate's nature plays an important role in the crystallisation process. Deposition on a conductive substrate may not necessarily be following the trends observed for a non-conductive substrate, e.g. glass.

In multiple recent publications, TiO$_2$ was produced by magnetron sputtering using small (4–8 cm diameter) metallic target [51,56–58]. These target sizes are not fit for high-volume industrial processes. Our results were obtained using a 300 × 100 mm metallic target, in a large chamber without substrate bias [20], radio frequency power supplies [20,21], substrate heating [22] or post-annealing [23–25], keeping the deposition process simple and reproducible. Our methodology could easily be replicated and scaled up for high-volume
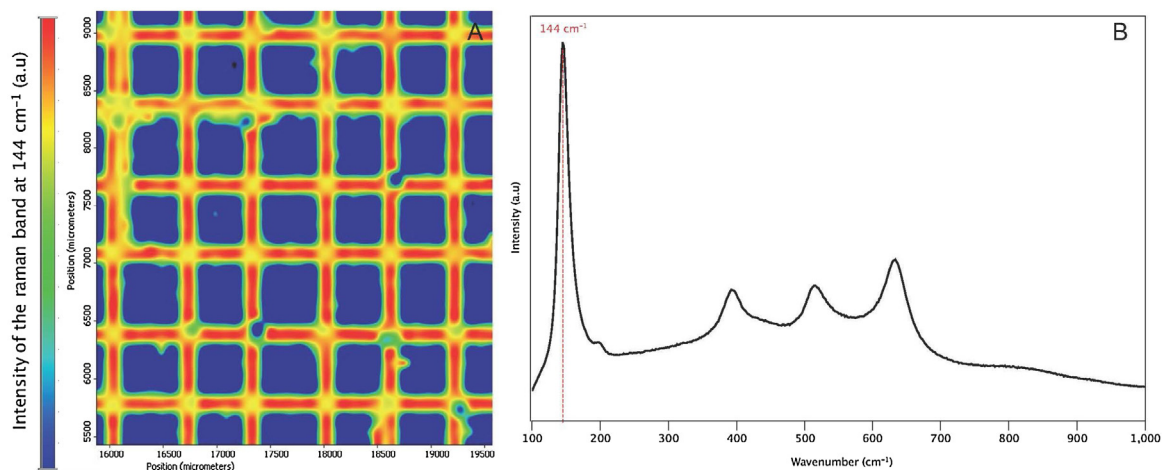
Fig. 11 – Raman mapping of an optimised TiO₂ coated mesh by magnetron sputtering at 1000 W – 0.44 Pa (left) and corresponding Raman spectrum (right).
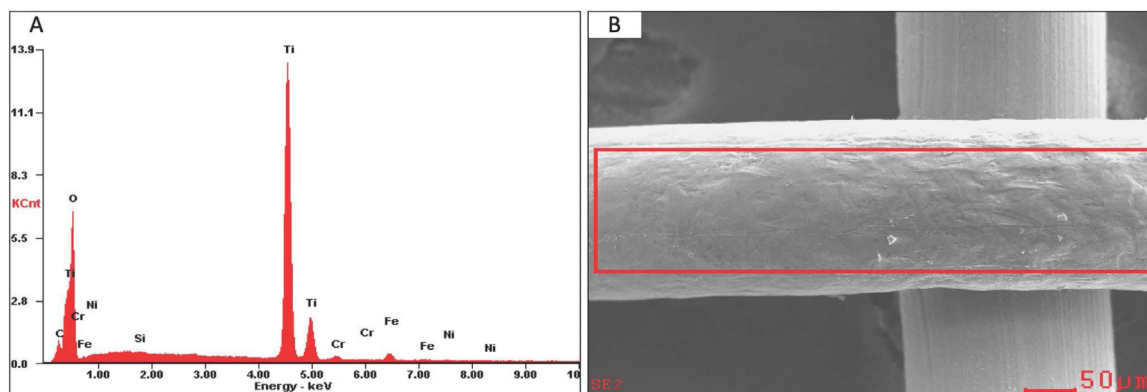

Fig. 12 – EDX spectra (A) of a stainless-steel thread coated by magnetron sputtering with TiO₂ at 1000 W – 0.44 Pa and corresponding SEM micrograph (B).
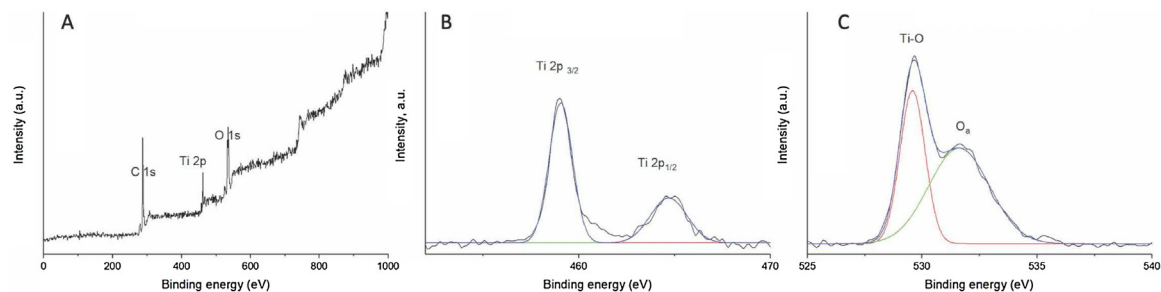

Fig. 13 – Selected XPS spectra of titanium dioxide coatings: A – survey spectrum of sample No. 10; B – Ti 2p spectrum of sample No. 10; C – O 1s spectrum of sample No. 10.

production of photocatalytically active TiO₂ supported on stainless steel mesh.

However, TiO₂ still suffers from its large band-gap and charge carrier recombination rate [3]. Therefore, we believe that follow up work should aim at addressing its shortcomings, while keeping the production process simple and economically friendly. Additionally, the semi-transparent nature of this substrate/catalyst combination means that there is a limit of to the number of mesh that can be stacked in a photocatalytic reactor. To maximise quantum yield, it will have to be taken into consideration when designing a photocatalytic reactor. Finally, although no corrosion was observed during our tests, the substrate has yet to be tested in a severe environment, more representative of real-world conditions.

5.   Conclusion

In summary, crystallised titanium dioxide was successfully grown onto stainless-steel mesh in a one-step process by
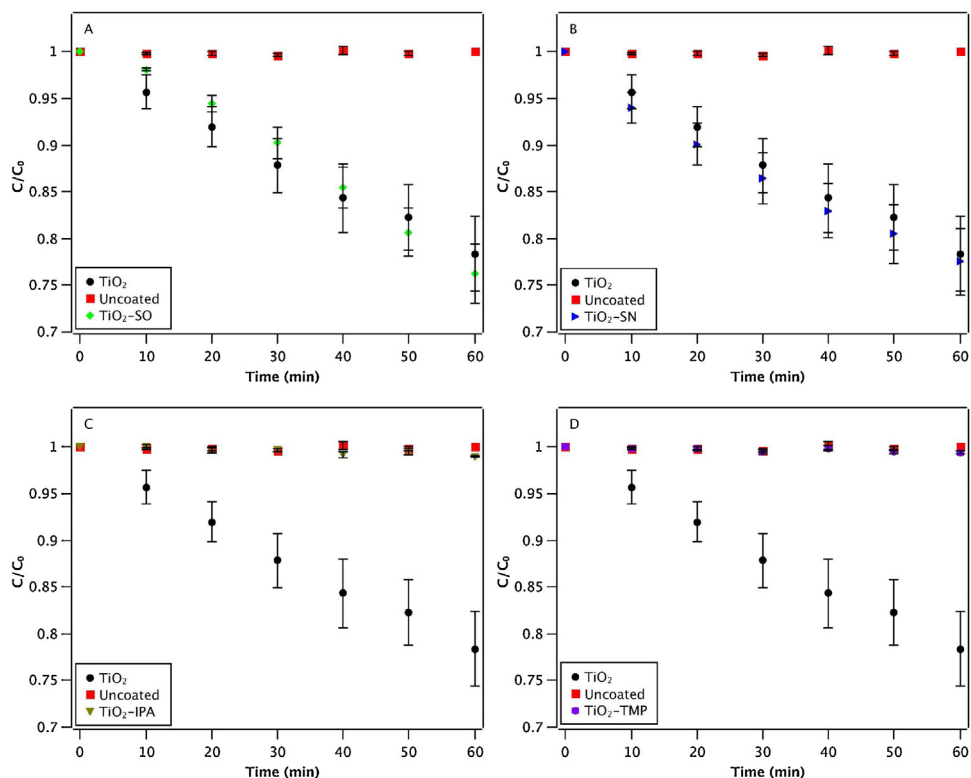
Fig. 14 – MO degradation under UV-A light by mesh coated with TiO$_2$ under optimised conditions of 1000 W and 0.44 Pa in the presence of h$^+$(A), e$^-$ (B), O$_2$$^{-\bullet}$ (C) and $\bullet$OH (D) scavengers.
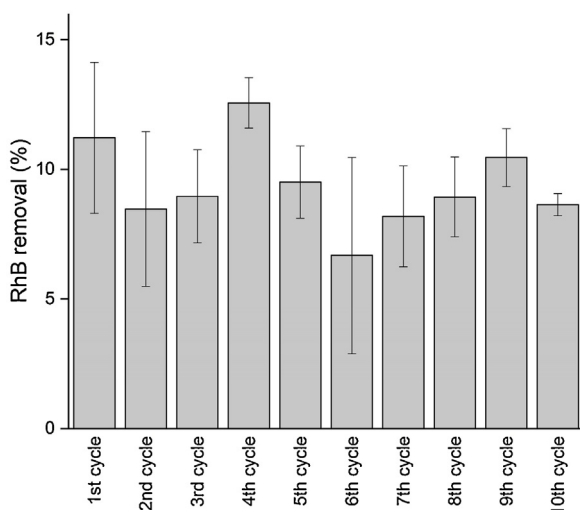

Fig. 15 – Cycling test of optimised sample No. 10 (1000 W – 0.44 Pa) for RhB degradation under UV-A for 1 h.

pulsed DC magnetron sputtering without annealing, substrate heating, substrate bias or additional energy sources. This one-step process production of crystallised TiO$_2$ thin film on stainless steel is industry friendly. High sputtering power was identified as essential, to obtain photocatalytically active crystalline TiO$_2$, on stainless steel mesh. On the other hand, increasing the pressure seemed to hinder the crystallisation process and had to be kept to a minimum. Methylene blue,

methyl orange and rhodamine B, the three most common types of dye used in the photocatalysis field, were successfully degraded under UV-A, by the TiO$_2$ coated stainless steel mesh. The scavenger test revealed that the degradation mechanism seemed to be mainly superoxide and hydroxide radical driven. Finally, the reusability of the coated mesh has been demonstrated with little to no photocatalytic activity loss after 10 consecutive cycles. Therefore, this substrate/coating combination seems to be a good fit for a high scale production of affordable stainless-steel mesh-based photocatalytic reactors.

Conflict of interest

The authors declare no conflicts of interest.

Appendix A. Supplementary data

Supplementary material related to this article can be found, in the online version, at doi:https://doi.org/10.1016/j.jmrt.2020.03.101.

REFERENCES

[1] "WHO | Progress on drinking water, sanitation and hygiene, WHO". [Online]. Available: http://www.who.int/water_sanitation_health/publications/jmp-2017/en/.
[2] "WASHwatch.org - 289,000 children die every year from diarrhoeal diseases caused by poor WASH." [Online].

Available: https://washwatch.org/en/blog/child-deaths-diarrhoeal-diseases-caused-poor-wash/.

[3] Byrne C, Subramanian G, Pillai SC. Recent advances in photocatalysis for environmental applications. J Environ Chem Eng 2017;(Aug), http://dx.doi.org/10.1016/j.jece.2017.07.080.

[4] Fujishima A, Honda K. Electrochemical photolysis of water at a semiconductor electrode. Nature 1972;238(Jul (5358)):37–8.

[5] Kiarii EM, Govender KK, Ndungu PG, Govender PP. The generation of charge carriers in semi conductors – a theoretical study. Chem Phys Lett 2017;678 Supplement C:167–76, http://dx.doi.org/10.1016/j.cplett.2017.04.051.

[6] Won Y, Schwartzenberg K, Gray KA. TiO2-based transparent coatings create self-cleaning surfaces. Chemosphere 2018;208(Oct):899–906, http://dx.doi.org/10.1016/j.chemosphere.2018.06.014.

[7] Sangchay W. The self-cleaning and photocatalytic properties of TiO2 doped with SnO2 thin films preparation by sol-gel method. Energy Procedia 2016;89(Jun):170–6, http://dx.doi.org/10.1016/j.egypro.2016.05.023.

[8] Shiva Kumar S, Ramakrishna SUB, Krishna SV, Srilatha K, Devi BR, Himabindu V. Synthesis of titanium (IV) oxide composite membrane for hydrogen production through alkaline water electrolysis. South Afr J Chem Eng 2018;25(Jun):54–61, http://dx.doi.org/10.1016/j.sajce.2017.12.004.

[9] Xu F, Wang T, Chen H, Bohling J, Maurice AM, Wu L, et al. Preparation of photocatalytic TiO2-based self-cleaning coatings for painted surface without interlayer. Prog Org Coat 2017;113(Dec):15–24, http://dx.doi.org/10.1016/j.porgcoat.2017.08.005.

[10] Atli A, Atilgan A, Yildiz A. Multi-layered TiO2 photoanodes from different precursors of nanocrystals for dye-sensitized solar cells. Sol Energy 2018;173(Oct):752–8, http://dx.doi.org/10.1016/j.solener.2018.08.027.

[11] Paz Y. Application of TiO2 photocatalysis for air treatment: patents' overview. Appl Catal B Environ 2010;99(Sep (3)):448–60, http://dx.doi.org/10.1016/j.apcatb.2010.05.011.

[12] Shinde PS, Bhosale CH. Properties of chemical vapour deposited nanocrystalline TiO2 thin films and their use in dye-sensitized solar cells. J Anal Appl Pyrolysis 2008;82(May (1)):83–8, http://dx.doi.org/10.1016/j.jaap.2008.01.004.

[13] Valencia S, Marín JM, Restrepo G. Study of the bandgap of synthesized titanium dioxide nanoparticules using the sol-gel method and a hydrothermal treatment. Open Mater Sci J 2009;4(Jun (1)).

[14] Yamamoto S, Sumita T, Sugiharuto, Miyashita A, Naramoto H. Preparation of epitaxial TiO2 films by pulsed laser deposition technique. Thin Solid Films 2001;401(Dec (1)):88–93, http://dx.doi.org/10.1016/S0040-6090(01)01636-4.

[15] Seo YG, Kim MA, Lee H, Lee W. Solution processed thin films of non-aggregated TiO2 nanoparticles prepared by mild solvothermal treatment. Sol Energy Mater Sol Cells 2011;95(Jan (1)):332–5, http://dx.doi.org/10.1016/j.solmat.2010.05.023.

[16] Lee H, Park Y-K, Kim S-J, Kim B-H, Jung S-C. Fe-decorated TiO2 powder photocatalysts with enhanced visible-light-driven degradation activities. Surf Coat Technol 2016;307(Dec):1018–23, http://dx.doi.org/10.1016/j.surfcoat.2016.08.033.

[17] Matos J, Miralles-Cuevas S, Ruíz-Delgado A, Oller I, Malato S. Development of TiO2-C photocatalysts for solar treatment of polluted water. Carbon 2017;122(Oct):361–73, http://dx.doi.org/10.1016/j.carbon.2017.06.091.

[18] Lee S-Y, Park S-J. TiO2 photocatalyst for water treatment applications. J Ind Eng Chem 2013;19(Nov (6)):1761–9, http://dx.doi.org/10.1016/j.jiec.2013.07.012.

[19] Kelly PJ, Arnell RD. Magnetron sputtering: a review of recent developments and applications. Vacuum 2000;56(Mar (3)):159–72, http://dx.doi.org/10.1016/S0042-207X(99)00189-X.

[20] Nezar S, et al. Properties of TiO2 thin films deposited by rf reactive magnetron sputtering on biased substrates. Appl Surf Sci 2017;395(Feb):172–9, http://dx.doi.org/10.1016/j.apsusc.2016.08.125.

[21] Song PK, Irie Y, Shigesato Y. Crystallinity and photocatalytic activity of TiO2 films deposited by reactive sputtering with radio frequency substrate bias. Thin Solid Films 2006;496(Feb (1)):121–5, http://dx.doi.org/10.1016/j.tsf.2005.08.249.

[22] Davi∂sdóttir S, Shabadi R, Galca AC, Andersen IH, Dirscherl K, Ambat R. Investigation of DC magnetron-sputtered TiO2 coatings: effect of coating thickness, structure, and morphology on photocatalytic activity. Appl Surf Sci 2014;313(Sep):677–86, http://dx.doi.org/10.1016/j.apsusc.2014.06.047.

[23] Singh J, Khan SA, Shah J, Kotnala RK, Mohapatra S. Nanostructured TiO2 thin films prepared by RF magnetron sputtering for photocatalytic applications. Appl Surf Sci 2017;422(Nov):953–61, http://dx.doi.org/10.1016/j.apsusc.2017.06.068.

[24] Cruz MRA, Sanchez-Martinez D, Torres-Martínez LM. Optical properties of TiO2 thin films deposited by DC sputtering and their photocatalytic performance in photoinduced process. Int J Hydrog Energy 2019;44(Jul (36)):20017–28, http://dx.doi.org/10.1016/j.ijhydene.2019.06.043.

[25] Lin Z-A, Lu W-C, Wu C-Y, Chang K-S. Facile fabrication and tuning of TiO2 nanoarchitectured morphology using magnetron sputtering and its applications to photocatalysis. Ceram Int 2014;40(Dec (10) Part A):15523–9, http://dx.doi.org/10.1016/j.ceramint.2014.07.025.

[26] Ratova M, Klaysri R, Praserthdam P, Kelly PJ. Pulsed DC magnetron sputtering deposition of crystalline photocatalytic titania coatings at elevated process pressures. Mater Sci Semicond Process 2017;71(Nov):188–96, http://dx.doi.org/10.1016/j.mssp.2017.07.028.

[27] Fernández-García A, Zarza E, Valenzuela L, Pérez M. Parabolic-trough solar collectors and their applications. Renew Sustain Energy Rev 2010;14(Sep (7)):1695–721, http://dx.doi.org/10.1016/j.rser.2010.03.012.

[28] Dillert R, Cassano AE, Goslich R, Bahnemann D. Large scale studies in solar catalytic wastewater treatment. Catal Today 1999;54(Dec (2)):267–82, http://dx.doi.org/10.1016/S0920-5861(99)00188-1.

[29] Anwer H, Mahmood A, Lee J, Kim K-H, Park J-W, Yip ACK. Photocatalysts for degradation of dyes in industrial effluents: opportunities and challenges. Nano Res 2019;(Jan), http://dx.doi.org/10.1007/s12274-019-2287-0.

[30] Ratova M, West GT, Kelly PJ. Optimisation of HiPIMS photocatalytic titania coatings for low temperature deposition. Surf Coat Technol 2014;250(Jul):7–13, http://dx.doi.org/10.1016/j.surfcoat.2014.02.020.

[31] Zhao W, et al. A novel Z-scheme Ag3VO4/BiVO4 heterojunction photocatalyst: study on the excellent photocatalytic performance and photocatalytic mechanism. Appl Catal B Environ 2019;245(May):448–58, http://dx.doi.org/10.1016/j.apcatb.2019.01.001.

[32] Liu Q, Guo Y, Chen Z, Zhang Z, Fang X. Constructing a novel ternary Fe(III)/graphene/g-C3N4 composite photocatalyst with enhanced visible-light driven photocatalytic activity via interfacial charge transfer effect. Appl Catal B Environ 2016;183(Apr):231–41, http://dx.doi.org/10.1016/j.apcatb.2015.10.054.

[33] Liang J, et al. Constructing high-efficiency photocatalyst for degrading ciprofloxacin: Three-dimensional visible light driven graphene based NiAlFe LDH. J Colloid Interface Sci

2019;540(Mar):237–46, http://dx.doi.org/10.1016/j.jcis.2019.01.011.

[34] Gupta R, Boruah B, Modak JM, Madras G. Kinetic study of Z-scheme C3N4/CuWO4 photocatalyst towards solar light inactivation of mixed populated bacteria. J Photochem Photobiol Chem 2019;372(Mar):108–21, http://dx.doi.org/10.1016/j.jphotochem.2018.08.035.

[35] Ding K, Wang W, Yu D, Wang W, Gao P, Liu B. Facile formation of flexible Ag/AgCl/polydopamine/cotton fabric composite photocatalysts as an efficient visible-light photocatalysts. Appl Surf Sci 2018;454(Oct):101–11, http://dx.doi.org/10.1016/j.apsusc.2018.05.154.

[36] Liu N, et al. Superior disinfection effect of Escherichia coli by hydrothermal synthesized TiO2-based composite photocatalyst under LED irradiation: influence of environmental factors and disinfection mechanism. Environ Pollut 2019;247(Apr):847–56, http://dx.doi.org/10.1016/j.envpol.2019.01.082.

[37] Deng W, et al. Visible-light-driven photocatalytic degradation of organic water pollutants promoted by sulfite addition. Environ Sci Technol 2017;51(Nov (22)):13372–9, http://dx.doi.org/10.1021/acs.est.7b04206.

[38] Chiu Y-H, Chang T-FM, Chen C-Y, Sone M, Hsu Y-J. Mechanistic insights into photodegradation of organic dyes using heterostructure photocatalysts. Catalysts 2019;9(May (5)):430, http://dx.doi.org/10.3390/catal9050430.

[39] Gautam A, Kshirsagar A, Biswas R, Banerjee S, Khanna PK. Photodegradation of organic dyes based on anatase and rutile TiO2 nanoparticles. RSC Adv 2016;6(Jan (4)):2746–59, http://dx.doi.org/10.1039/C5RA20861K.

[40] Bharti B, Kumar S, Lee H-N, Kumar R. Formation of oxygen vacancies and Ti^{3+} state in TiO_2 thin film and enhanced optical properties by air plasma treatment. Sci Rep 2016;6(Aug):32355, http://dx.doi.org/10.1038/srep32355.

[41] Zhou B, Jiang X, liu Z, Shen R, Rogachev AV. Preparation and characterization of TiO2 thin film by thermal oxidation of sputtered Ti film. Mater Sci Semicond Process 2013;16(Apr (2)):513–9, http://dx.doi.org/10.1016/j.mssp.2012.05.001.

[42] Sønderby S, Christensen BH, Almtoft KP, Nielsen LP, Eklund P. Industrial-scale high power impulse magnetron sputtering of yttria-stabilized zirconia on porous NiO/YSZ fuel cell anodes. Surf Coat Technol 2015;281(Nov):150–6, http://dx.doi.org/10.1016/j.surfcoat.2015.09.058.

[43] Alfonso E, Olaya J, Cubillos G. Thin film growth through sputtering technique and its application. Cryst- Sci Technol 2012;(Sep), http://dx.doi.org/10.5772/35844.

[44] Konuma M. Film deposition by plasma techniques. Berlin Heidelberg: Springer-Verlag; 1992.

[45] Yang L, et al. Effect of annealing temperature on wettability of TiO2 nanotube array films. Nanoscale Res Lett 2014;9(Nov (1)):621, http://dx.doi.org/10.1186/1556-276X-9-621.

[46] Taherniya A, Raoufi D. The annealing temperature dependence of anatase TiO2thin films prepared by the electron-beam evaporation method. Semicond Sci Technol

2016;31(Nov (12)):125012, http://dx.doi.org/10.1088/0268-1242/31/12/125012.

[47] Wang B, et al. Morphology, structure and optical properties in TiO_2 nanostructured films annealed at various temperatures: publisher's note. Opt Mater Express 2015;5(Nov (11)), http://dx.doi.org/10.1364/OME.5.002545, 2545–2545.

[48] Bakri AS, et al. Effect of annealing temperature of titanium dioxide thin films on structural and electrical properties. AIP Conf Proc 2017;1788(Jan (1)):030030, http://dx.doi.org/10.1063/1.4968283.

[49] Ma Y-J, Lu F, Xiang B-X, Zhao J-L, Ruan S-C. Fabrication of TiO_2 thin films with both anatase and rutile structures together using the ion-implantation method. Opt Mater Express 2018;8(Mar (3)):532–40, http://dx.doi.org/10.1364/OME.8.000532.

[50] Zhang C, Ding W, Wang H, Chai W, Ju D. Influences of working pressure on properties for TiO2 films deposited by DC pulse magnetron sputtering. J Environ Sci 2009;21(Jan (6)):741–4, http://dx.doi.org/10.1016/S1001-0742(08)62334-7.

[51] Wang B, et al. Effect of deposition parameters on properties of TiO2 films deposited by reactive magnetron sputtering. Ceram Int 2017;43(Oct (14)):10991–8, http://dx.doi.org/10.1016/j.ceramint.2017.05.139.

[52] Fujishima A, Zhang X, Tryk DA. TiO2 photocatalysis and related surface phenomena. Surf Sci Rep 2008;63(Dec (12)):515–82, http://dx.doi.org/10.1016/j.surfrep.2008.10.001.

[53] Eufinger K, Janssen EN, Poelman H, Poelman D, De Gryse R, Marin GB. The effect of argon pressure on the structural and photocatalytic characteristics of TiO2 thin films deposited by d.c. Magnetron sputtering. Thin Solid Films 2006;515(Oct (2)):425–9, http://dx.doi.org/10.1016/j.tsf.2005.12.247.

[54] Pihosh Y, Goto M, Kasahara A, Tosa M. Photocatalytic property of TiO2 thin films sputtered-deposited on unheated substrates. Appl Surf Sci 2009;256(Nov (4)):937–42, http://dx.doi.org/10.1016/j.apsusc.2009.05.155.

[55] Liu B, Zhao X, Zhao Q, Li C, He X. The effect of O2 partial pressure on the structure and photocatalytic property of TiO2 films prepared by sputtering. Mater Chem Phys 2005;90(Mar (1)):207–12, http://dx.doi.org/10.1016/j.matchemphys.2004.10.038.

[56] Kozlovskiy A, Shlimas I, Dukenbayev K, Zdorovets M. Structure and corrosion properties of thin TiO2 films obtained by magnetron sputtering. Vacuum 2019;164(Jun):224–32, http://dx.doi.org/10.1016/j.vacuum.2019.03.026.

[57] Nuñez JAP, Salapare HS, Villamayor MMS, Siringan MAT, Ramos HJ. Antibacterial efficiency of magnetron sputtered TiO2 on poly(methyl methacrylate). Surf Interfaces 2017;8(Sep):28–35, http://dx.doi.org/10.1016/j.surfin.2017.04.003.

[58] Sorar I, Pehlivan E, Niklasson GA, Granqvist CG. Electrochromism of DC magnetron-sputtered TiO2: role of film thickness. Appl Surf Sci 2014;318(Nov):24–7, http://dx.doi.org/10.1016/j.apsusc.2013.12.015.